

GHz SAW strain sensors under high mechanical load conditions

MinHee Kwon* , Matthias Schlögl , Daniel Platz  and Ulrich Schmid 

Institute of Sensor and Actuator Systems, TU Wien, 1040 Vienna, Austria

E-mail: minhee.kwon@tuwien.ac.at

Received 5 November 2024, revised 13 December 2024

Accepted for publication 30 January 2025

Published 12 February 2025



Abstract

Strain sensors have been developed in various fields by converting mechanical deformation into electrical signals. Surface acoustic wave (SAW) devices are beneficial for strain sensing due to their simplicity of fabrication and wireless operation capabilities. In this study, we investigate SAW strain sensors operating at 1.25 GHz. The fabricated SAW resonators using standard photolithography technology are characterized with a custom-made cantilever setup capable of applying defined strain values up to approximately $-4000 \mu\epsilon$ to $4000 \mu\epsilon$. From these measurements, a high responsivity even up to this high strain values is demonstrated. We also explore the impact of geometric design parameters on strain-sensing performance. We vary the length of the SAW resonator and observe that the longer the SAW resonator, the more responsive the device gets to strain changes. When the distance between the two reflectors confining the SAW is $2207 \mu\text{m}$, the responsivity to strain is $114.99 \text{ Hz } \mu\epsilon^{-1}$. In summary, this study investigates the feasibility of GHz SAW resonators as high-strain sensors on non-flexible substrates with a custom-built experimental setup, to evaluate their potential for future applications in extreme mechanical environments.

Keywords: surface acoustic waves (SAW), strain sensor, GHz frequency, frequency shift, resonator length, mechanical strain

1. Introduction

Strain sensors that convert mechanical deformation into electrical signals are widely researched and utilized in fields such as civil and architectural engineering, automotive and aerospace, and the medical device industry [1]. High-sensitivity strain sensors can be expensive due to complex manufacturing processes. For example, micro-strain sensitive devices based on fiber-optical transducers [2–4] and capacitive

transducers [1, 5–7] require intricate manufacturing techniques. However, advancements in batch-compatible complementary metal–oxide–semiconductor (CMOS) technology have significantly reduced costs, enabling mass production with high precision and consistency. Surface acoustic wave (SAW) sensors, which can also be fabricated with CMOS technology [8–10], offer additional advantages. They are simpler to manufacture, requiring only a layer of piezoelectric material on a substrate and interdigital transducers (IDTs). Moreover, SAW strain sensors are low-power devices that offer the potential for wireless operation [11–14].

When strain is applied to a SAW sensor, both the length and the elastic modulus of the substrate get modified, causing the path and propagation velocity of the SAW to change. This results in a shift in the frequency and phase of the reflected waves. SAW strain sensors provide high sensitivity and fast response times [15–19], making them suitable for real-time monitoring of strain variations [20–22]. However, a drawback of SAW strain sensors is their cross-sensitivity to temperature

* Author to whom any correspondence should be addressed.



Original Content from this work may be used under the terms of the [Creative Commons Attribution 4.0 licence](https://creativecommons.org/licenses/by/4.0/). Any further distribution of this work must maintain attribution to the author(s) and the title of the work, journal citation and DOI.

changes, which affects the accuracy of the strain measurements, necessitating the use of materials with minimal temperature sensitivity and comparable thermal coefficients of expansion (TCE). Aluminum nitride (AlN) is an excellent choice for SAW strain sensors due to its thermal properties. AlN has a TCE of $4.2 \times 10^{-6} \text{ }^\circ\text{C}^{-1}$ [23] and temperature coefficient of frequency (TCF) of $-25 \text{ ppm }^\circ\text{C}^{-1}$ [24, 25]. In comparison, lithium niobate (LiNbO₃) and zinc oxide (ZnO) have TCFs of -58 to $-90 \text{ ppm }^\circ\text{C}^{-1}$ and $-60 \text{ ppm }^\circ\text{C}^{-1}$, respectively [15, 24]. Thus, AlN is relatively less affected by temperature. Even more, the high sound velocity of AlN, above 5000 m s^{-1} enables the realization of high frequency SAWs in the GHz range [9, 26], such as those in the GHz range. Shorter wavelengths at GHz frequencies allow for the design of more compact as well as lightweight sensors. In fact, SAW strain sensors operating at high frequencies such as around 900 MHz and 4 GHz have been researched [27–29], particularly in wireless RF applications, where higher frequencies improve component compatibility.

Previous studies on SAW strain sensors on non-flexible substrates have focused mainly on a strain regime below $\pm 1000 \mu\epsilon$ [12, 30–37]. This limit is typically chosen to ensure that the sensors operate within the linear strain regime of the substrate materials, avoiding nonlinear effects and ensuring repeatable sensor operation. However, some studies have applied large strain values up to $1200 \mu\epsilon$ on non-flexible substrates [38] and up to $5000 \mu\epsilon$ on flexible substrates [21]. To the best of the authors' knowledge, however, SAW strain sensors on non-flexible (i.e. mechanically rigid) substrates were not characterized up to $\pm 4000 \mu\epsilon$ so far [20, 21, 39]. To fully exploit their performance for future applications, the sensing performance of these devices is evaluated beyond the standard strain regime. Furthermore, few studies have investigated how geometric design parameters affect the strain-sensing capability under such high mechanical loads [17, 40]. These studies have examined geometric design parameters, such as the piezoelectric material's thickness or the IDT electrodes' width. However, the effect of resonator length on strain-sensing performance is still not investigated.

In this study, we fabricate AlN SAW resonators operating in the GHz range for strain sensing. We use a custom-designed experimental setup, integrating a cantilever system capable of applying controlled mechanical strain values, thus allowing us to investigate its impact on the resonance frequency shift of the fabricated SAW resonators. For this purpose, the GHz SAW resonators are fixed to a bendable cantilever capable of applying different strain values under defined mechanical loading conditions up to approximately $\pm 4000 \mu\epsilon$. Even more, we also measure the response to strain changes of various GHz SAW resonators with different resonator lengths but keep the other design parameters constant for reasons of comparison. Our primary aim is to demonstrate the feasibility of SAW strain sensing under high mechanical loads and understand how resonator length influences strain responsiveness, rather than optimizing sensor performance, which would require different design trade-offs. These insights lay the foundation for the future development of GHz SAW strain

sensors for applications such as structural health monitoring and aerospace systems, where high responsivity and robustness are essential.

2. Experimental details

2.1. Fabrication process

SAW resonators using AlN with frequencies in the GHz range are fabricated by optical photolithography with a line and a space width of $1 \mu\text{m}$, as reported in [26]. Figures 1(a)–(h) shows the fabrication process of GHz SAW resonators starting with a pure silicon (Si) wafer with a thickness of $360 \mu\text{m}$. AlN thin films with a thickness of $1.4 \mu\text{m}$ are sputter-deposited using a DC magnetron sputtering system, LS730S (Von Ardenne) at a chamber pressure of $2 \mu\text{bar}$ in a pure nitrogen atmosphere with a constant flow rate of 50 sccm and plasma power of 800 W . AlN synthesized through a similar deposition process exhibits piezoelectric coefficients of $d_{33} = 3.15 \text{ pm V}^{-1}$ and $d_{31} = 1.28 \text{ pm V}^{-1}$ for a film thickness exceeding 100 nm [41]. We use an aluminum (Al) disk with a diameter of 6.0 inches as a sputter target with a substrate-to-target distance of 65 mm. Next, the SAW resonator on the AlN film operates in resonance frequencies above 1 GHz, with a SAW wavelength of $4 \mu\text{m}$, and an IDT electrode width designed to be $1 \mu\text{m}$. The photoresist (AZ5214) in diluted propylene glycol monomethyl ether acetate is spin-coated onto the AlN layer with a thickness of about 560 nm . The photoresist film is then sequentially exposed to UV light by an MLA 150 (Maskless Aligner) and developed to pattern the SAW resonators. Afterward, we deposit an Al metal layer with a thickness of 140 nm and a capping layer of gold (Au) with a thickness of 10 nm to prevent oxidation of the Al layer. The latter layer stack is lifted off by dipping in acetone. Finally, the wafer is diced, resulting in individual devices.

Figure 1(i) shows the fabricated SAW device under an optical microscope. The IDT is centered with two reflectors placed equidistantly on either side. The reflectors, separated by a distance d_r , confine the SAWs generated by the IDT and determine the resonator length. The additional electrode descending from one of the busbars connected to the IDT fingers is directly connected to the electrode pad through a coplanar waveguide line. In this study, we investigate three different SAW resonator designs, as shown in table 1. All designs have the same number of electrode finger pairs in IDT N_p , the number of grating electrodes in a reflector N_g , the SAW wavelength λ , the electrode width p , and the transverse IDT electrode width W . The only difference is the distance between the two reflectors d_r : device 1 with $d_{r1} = 685 \mu\text{m}$, device 2 with $d_{r2} = 1205 \mu\text{m}$, and device 3 with $d_{r3} = 2207 \mu\text{m}$. We fabricate these three devices to study how strain sensing depends on the resonator length.

2.2. Measurement setup

The concept of experimental setup involves applying strain to a GHz SAW resonator attached to a cantilever and monitoring

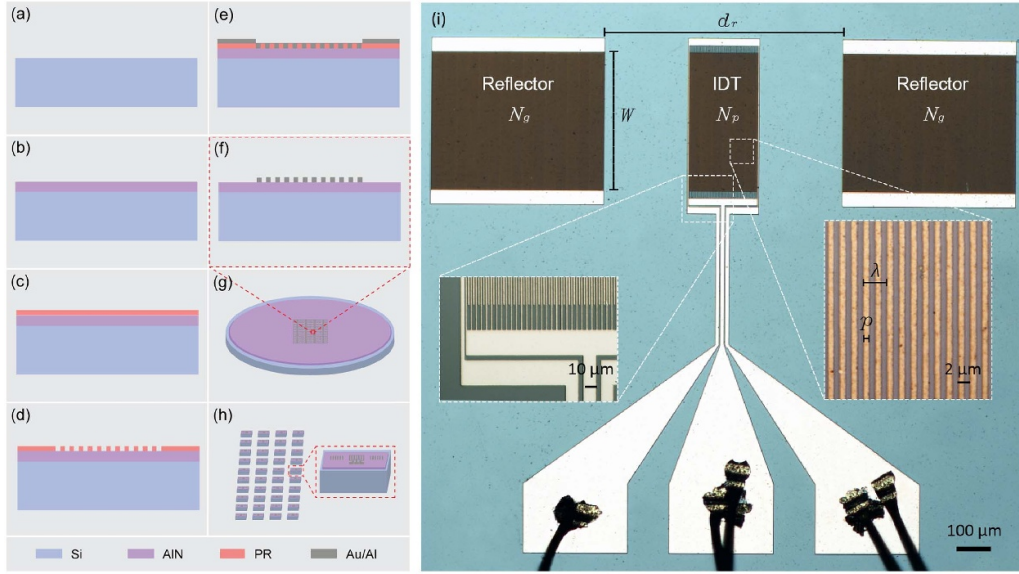


Figure 1. (a)–(h) Schematics of the fabrication process for the GHz SAW devices. (a) Preparation of a cleaned pure silicon (Si) wafer. (b) Sputter-deposition of AlN film. (c) Coated photoresist film. (d) UV exposure and development process for SAW structure patterns. (e) Evaporation of Au/Al. (f) Lift-off process. (g) The wafer after process (a)–(f). (h) Obtained devices after dicing the wafer. (i) Optical micrograph of an actual device. The IDT is placed in the middle between two reflectors called distributed Bragg mirrors. The geometric parameters of the SAW strain device are: wavelength of SAW λ , width of IDT and grating electrodes p , number of IDT electrode pairs N_p , number of reflector's electrodes N_g , width of transverse IDT electrodes W , the distance between two reflectors d_r . Electrode pads are placed below IDT by designing a coplanar waveguide (CPW) transmission line. The pads are connected from the busbar of the IDT. Some contamination spots near the electrode pads are removed for clarity.

Table 1. Geometric design parameters of the three SAW resonators. The three SAW resonators (Device 1, Device 2, and Device 3) have identical geometric parameters (λ , p , N_p , N_g , and W) except for the distance between the reflectors (d_r). The parameter d_r for each resonator is labeled as d_{r1} , d_{r2} , and d_{r3} respectively.

Fixed geometric parameters	
N_p	50
N_g	250
λ	4 μm
p	1 μm
W	400 μm
Variable geometric parameter d_r	
Device 1: d_{r1}	685 μm
Device 2: d_{r2}	1205 μm
Device 3: d_{r3}	2207 μm

shifts in resonance frequency [42]. Strain is applied by bending the cantilever tip, and the corresponding strain value is calculated using the Euler–Bernoulli beam theory. The resonance frequency is then extracted from S_{11} measurements using a vector network analyzer (VNA), allowing us to evaluate the sensor's responsivity to strain.

The entire setup is shown in figure 2. The SAW device and a custom-made printed circuit board (PCB) are directly glued onto the cantilever with an EC101 two-component resin from Polytec as shown in figure 2(a). The cantilever is made of Al with length L of 200 mm and thickness h_c of 3 mm. The

thickness of the Si wafer used as the device substrate, the thickness of the deposited AlN, and the thickness of the electrode metal are about 360 μm , 1.4 μm , and 0.15 μm , respectively. Therefore, the total thickness of the chip h_s is about 362 μm . A defined strain ε can be applied to a SAW device depending on the tip displacement of the cantilever d_c at the position of the device x_0 . The device contains a SAW resonator, and the center position of the SAW resonator is x_0 as shown in figure 2(a). The position-dependent strain ε is given by the equation

$$\varepsilon = -\frac{3 d_c (h_c + 2h_s)}{2 L^3} (L - x_0), \quad (1)$$

which is based on Euler–Bernoulli beam theory [42, 44]. When the cantilever is bent down with a negative value of d_c , the SAW device experiences tensile strain ε with a positive sign. Conversely, if the cantilever bends upward with a positive value of d_c , the SAW device is subject to compressive strain ε with a negative sign. The displacement of the cantilever tip is automated by Stepperonline's Nema 17 stepper motor, shown in figure 2(b). This motor driver board is controlled by an Arduino Mega, which includes a motor driver board that is controlled by a Python script. The spindle, rotated by the stepper motor, has a pitch of 1 mm/rev. and provides an overall resolution of 0.05 rev., which corresponds to minimum tip displacement of 0.25 mm. The tip displacement ranges from -30.00 to 30.00 mm [42]. For a device positioned at x_0 of 10.00 mm, strain values between $\pm 3979 \mu\text{e}$ can be reached.

Figure 3(a) shows the strain ε calculated by equation (1). When the positions of the device x_0 are 10.0, 30.0 and

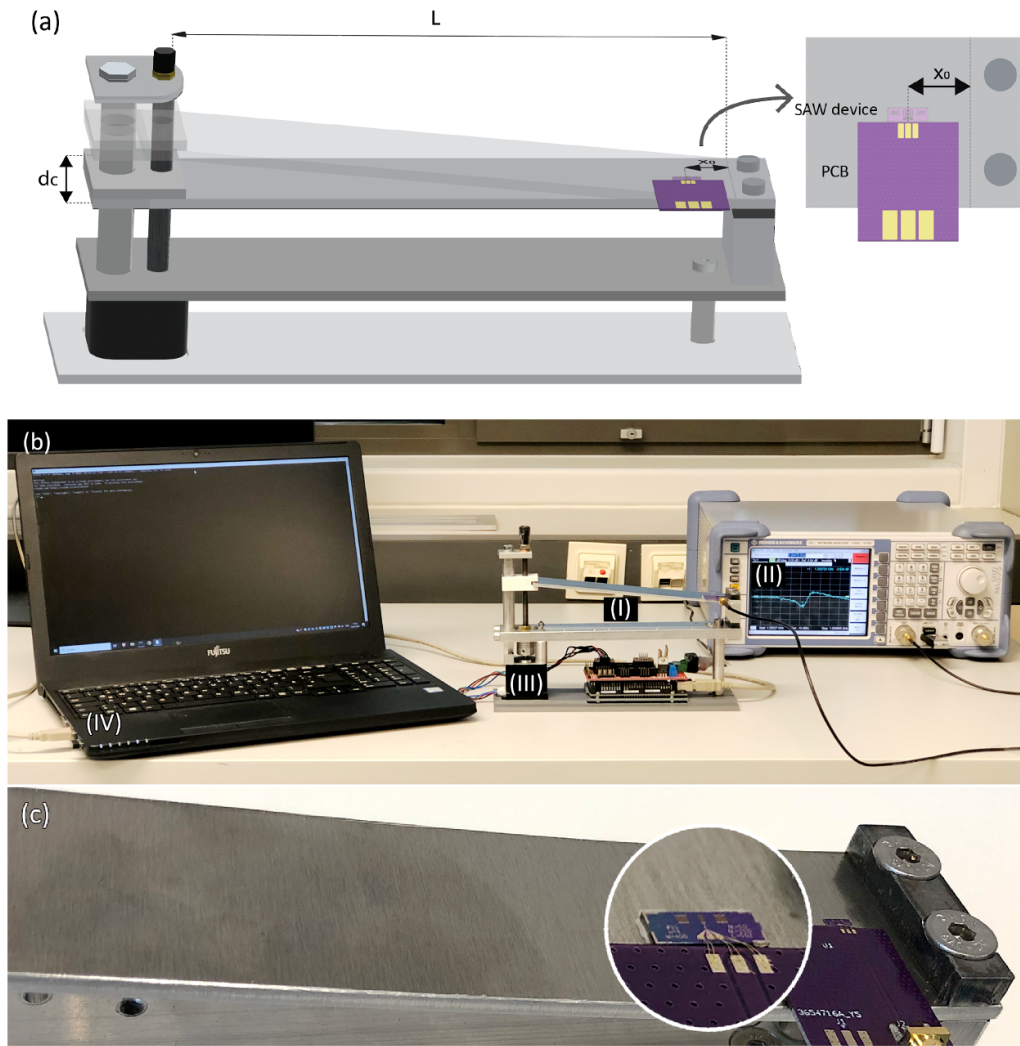


Figure 2. The strain measurement setup. (a) Schematic illustration of the key measurement setup with an Al cantilever, a SAW device, and a printed circuit board (PCB) as key components. When an Al cantilever with length L is bent, the cantilever tip displaces by d_c . The SAW device is glued on the Al cantilever at the position x_0 from the edge of the cantilever. The PCB is glued directly underneath the SAW device. Reproduced from [43]. © 2024 The Authors. CC BY 4.0. (b) The photo of the entire measurement setup including an Al cantilever (I) and a vector network analyzer (VNA) (II) to characterize the SAW devices. The cantilever is bent by a Nema 17 stepper motor (III) which is PC controlled (IV). This photo represents the real experimental configuration used to apply defined strain values to the SAW device and to monitor its frequency response. (c) The photo of the actual SAW device under mechanical load conditions.

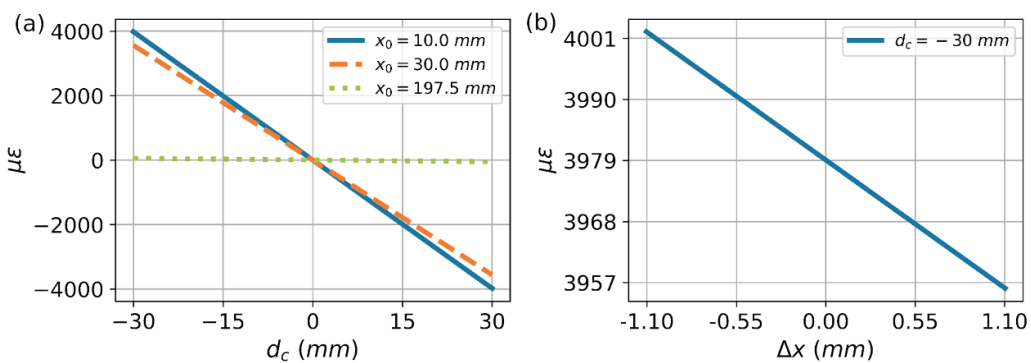


Figure 3. (a) Mechanical strain ϵ given by the cantilever tip displacement d_c at the position of strain sensor x_0 of 10.0, 30.0, and 197.5 mm. (b) Mechanical strain distribution depending on the location along the chip axis. The x -axis represents the relative position within the resonator, and the y -axis represents the strain value calculated at each location. When the SAW resonator is positioned at 1 mm, the central position inside the resonator is $\Delta x = 0.00$ mm.

197.5 mm, the tip displacement of the cantilever beam d_c is bent from -30 to 30 mm. In our setup, when the device is positioned at the maximum distance from the fixed end, $x_0 = 197.5$ mm, the strain ε that can be applied to the SAW resonator is between $\pm 52 \mu\epsilon$. When the positions of the device x_0 for SAW sensing experiments are 30.0 and 10.0 mm as from the fixed end, the applicable strain regimes are $\pm 3560 \mu\epsilon$ and $\pm 3979 \mu\epsilon$, respectively. Although the position of the device is fixed at x_0 , the applied strain ε is not perfectly homogeneous across the entire length of the SAW resonator. Figure 3(b) shows the distribution of local strain ε across the resonator length when the resonator is positioned at $x_0 = 10.0$ mm. The x -axis represents the relative position inside the SAW resonator length of 2.21 mm, and the center of the resonator is at $\Delta x = 0.00$ mm. The y -axis represents the strain ε at the point away from the center of the resonator Δx . When the strain ε applied to the center of the resonator is $3979 \mu\epsilon$, the strain ε applied to both ends of the resonator are $3995 \mu\epsilon$ and $4002 \mu\epsilon$, respectively, resulting in a strain error of up to 1.16% in the SAW resonator. The strains ε used in our experiments refer to the applied strain at the center of the resonator at the position on the cantilever x_0 . Due to minor variations in strain, this impact is regarded as negligible. Thus, the strain across the SAW resonator can be considered as uniform, primarily determined by the device position x_0 on the cantilever.

We characterize the SAW devices with reflection measurements using a (VNA, Rohde & Schwarz ZVL-6) as reported in [26]. The PCB glued onto the cantilever is connected to the metal pads on the SAW device by gold wire bonding. The transmission lines on the PCB are designed for a characteristic impedance of 50Ω and end in SubMiniature version A (SMA) connectors for connecting to the VNA. The VNA and the cable with the SMA connector are calibrated with a calibration kit (Rohde & Schwarz ZN-Z135). We use a full one-port calibration as in the short-open-match measurement for reflection measurements. With the VNA, we measure the reflection coefficient S_{11} of the devices as a function of frequency at room temperature. To minimize frequency changes due to temperature fluctuations during strain sensing measurements, the characterization is performed in a temperature-controlled laboratory maintained at room temperature (25 ± 1 °C). Figures 2(b) and (c) show the setup for SAW strain measurement including the Al cantilever and VNA. We measure the reflection coefficient S_{11} of the device 10 times and save the average value.

This experimental setup allows us to apply mechanical strain to the SAW resonator and measure the corresponding frequency shifts in real-time. Notably, this is the first study to investigate strain sensing in GHz SAW resonators under high strain regimes of up to approximately $-4000 \mu\epsilon$ to $4000 \mu\epsilon$ on non-flexible substrates. Furthermore, by designingly varying the resonator length, we aim to observe how geometric design parameters influence the performance of SAW strain sensors under high strain.

3. Result and discussion

3.1. GHz SAW resonators

In the reflection coefficient S_{11} spectrum of the SAW resonators, we define the resonance frequency as the minimum value of the magnitude of the reflection coefficient $|S_{11}|$. Figure 4(a) displays the magnitude of the reflection coefficient $|S_{11}|$ of a GHz SAW resonator without applied strain and not attached to an Al cantilever. The measured device in figure 4 is designed with the geometric parameters from table 1 as device 1. In the $|S_{11}|$ spectrum, several modes appear simultaneously depending on the resonator length. In our study, we define the frequency of the central mode as the resonance frequency of the SAW resonator. The difference between this resonance frequency and the adjacent modes is called the free spectral range (FSR). The minimum value of the reflection coefficient $|S_{11}|$ between 1.25 and 1.26 GHz is 1.25476 GHz. The differences between resonance frequency and the adjacent mode frequencies, FSR1 and FSR2, are 6.37 and 5.67 MHz, respectively. The single electrode reflectivity can be calculated with FSR2 which is closer to the resonance frequency [26, 45]. The single electrode reflectivity of the resonator we measure in figure 4 is 0.0127 , which is reasonable as for the SAW resonators reported in [45].

The impedance of the SAW resonator can be modeled with the Butterworth–Van Dyke equivalent circuit at the measurement ports. In this model, the reflection coefficient S_{11} can be calculated as

$$S_{11}(f) = \frac{(Q_e - Q_i)/Q_e + i(2Q_i(f - f_0))/f_0}{(Q_e + Q_i)/Q_e + i(2Q_i(f - f_0))/f_0}, \quad (2)$$

with the resonance frequency of the SAW resonator f_0 , the external quality factor Q_e , and the internal quality factor Q_i [26, 46]. We use equation (2) as a fit function of the measured reflection coefficient S_{11} to obtain the resonance frequency and quality factor Q . The total quality factor Q is obtained as the reciprocal value of the sum of the reciprocals of the external quality factor Q_e and the internal quality factor Q_i . Figure 4(b) shows the magnitude (green circles) and the phase (pink squares) of the measured reflection coefficient S_{11} as the zoomed-in SAW response of figure 4(a). The solid lines are fitted by using equation (2) resulting in 1.25476 GHz of resonance frequency, 4497 for the external quality factor Q_e , and 2690 for the internal quality factor Q_i . Thus, the total quality factor Q is calculated as 1683 . This SAW resonator has a high quality factor compared to geometrically similar devices, resulting in a high Qf product of 1.2×10^{12} Hz [26, 47–49]. Next, we analyze the data by applying strain to the SAW resonator, using the same fitting procedure to extract the resonance frequency as a function of external mechanical strain.

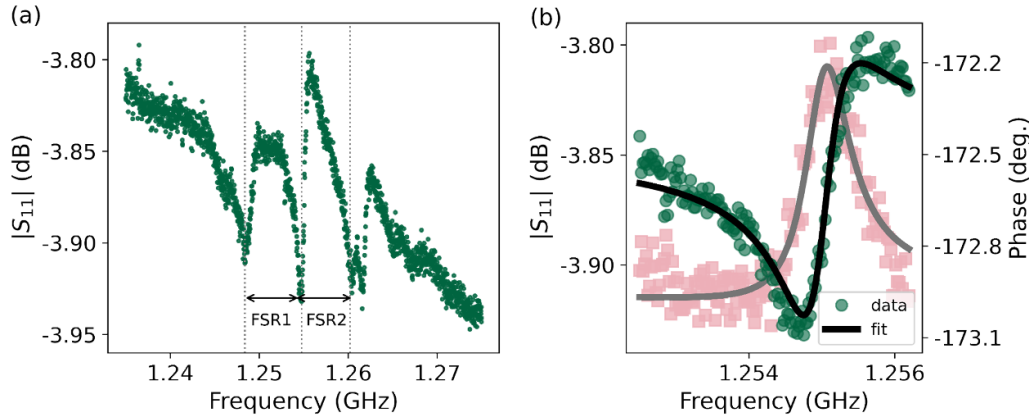


Figure 4. (a) Measured magnitude of reflection coefficient S_{11} from the fabricated SAW resonator without applied strain. When the middle minimum represents is the resonance frequency, the length between adjacent dips is indicated as the neighboring minima to the left and right represent FSR1 and FSR2. (b) Central signal of the reflection coefficient S_{11} in zoomed-in view around the resonance frequency. The green circles represent the magnitude, and the pink squares represent the phase of the reflection coefficient S_{11} . The solid lines are the fitting curve from equation (2).

3.2. Frequency shift under high strain conditions

Figure 5(a) shows the magnitude of reflection coefficient $|S_{11}|$ spectrum of Deive 1 as a function of the Al cantilever tip displacement d_c at $x_0 = 30.0$ mm and the device measured is the same resonator characterized in figure 4. To visually notice the shift in the SAW response as the displacement of the cantilever tip varies by 5 mm, the response, magnitude of reflection coefficient $|S_{11}|$ is deliberately offset. When the tip displacement d_c is 0, and no external strain is applied, the magnitude of reflection coefficient $|S_{11}|$ is positioned at 0.0 dB and each data set is shifted by 0.1 dB according to the displacement value d_c . As compressive strain is applied, the resonance frequency of the SAW decreases, and as tensile strain is applied, the resonance frequency increases. When the cantilever is bent to its maximum displacement, $d_c = \pm 25$ mm, these two frequency values are connected by a black solid line as a guide to the eye.

As shown in figure 4, the resonance frequency of device 1 is 1.254 76 GHz before gluing the device to the Al cantilever. After gluing it to the Al cantilever and with the cantilever tip displacement $d_c = 0$ mm, the resonance frequency we measured is 1.254 87 GHz. The relative frequency shift at zero strain, calculated as the difference between these two resonance frequencies divided by the initial resonance frequency of 1.254 76 GHz, is approximately 0.008 76%. Therefore, the influence of the glue on the resonance frequency is less than about 0.01% and can be considered negligible. Hence, we consider the resonance frequency measured after gluing onto the Al cantilever, with $d_c = 0$ mm, as the zerostrain resonance frequency.

Figure 5(b) shows the frequency shift Δf under the applied strain range $\pm 3560 \mu\epsilon$ as blue circles from experimental data of figure 5(a). The frequency shift Δf on the y-axis is calculated by subtracting 1.254 87 GHz, the resonance frequency at zero strain, from the strained device resonance frequency obtained from the fit curve using equation (2). The result shows that the frequency shift is linear over the full strain

interval. The solid line is a linear function fitted to the data, and its slope is the SAW strain responsivity R , so this device has a responsivity R of $93.80 \text{ Hz } \mu\epsilon^{-1}$ which is higher by approximately 17% than the reported responsivity of $80.09 \text{ Hz } \mu\epsilon^{-1}$ achieved with a similar SAW resonator design [37].

3.3. Dependence on resonator length

A key parameter in the design of the SAW resonator is the resonator length which is defined by the position of the reflectors. The experimental data in figure 5 is obtained from the SAW resonator of Device 1 with $d_{r1} = 685 \mu\text{m}$. We perform experiments with SAW resonators of different lengths of $d_{r2} = 1205 \mu\text{m}$ and $d_{r3} = 2207 \mu\text{m}$, to evaluate the impact of resonator length. Both SAW resonators are designed according to the parameters in table 1 as device 2 and device 3. Additionally, we increase the strain range up to $\pm 3979 \mu\epsilon$ by placing the SAW resonators on the cantilever at the position $x_0 = 10.0$ mm and changing the displacement of cantilever tip d_c from -30.0 to 30.0 mm in steps of 2.5 mm. These two resonators with different resonator lengths are measured and data are fitted with the same procedure, as introduced above shown in figure 5(b).

Figures 6(a) and (b) demonstrate that the frequency shift trend remains similar over the full strain interval even within a large strain regime between $\pm 3979 \mu\epsilon$. The responsivities R of the SAW strain sensors for device 2 and device 3 are 100.48 and $114.99 \text{ Hz } \mu\epsilon^{-1}$. Interestingly, the results for SAW strain sensing with different resonator lengths show that the responsivity R to strain increases as the distance between two reflectors d_r increase, as shown in figure 6(c). The gray dashed line, representing the linear fit function of the responsivity R of the three devices, shows that for each $1 \mu\text{m}$ increase in resonator length d_r , the responsivity R increases by approximately $0.014 \text{ Hz } \mu\epsilon^{-1}$. This observation suggests that longer resonator lengths result in larger frequency shifts at a given

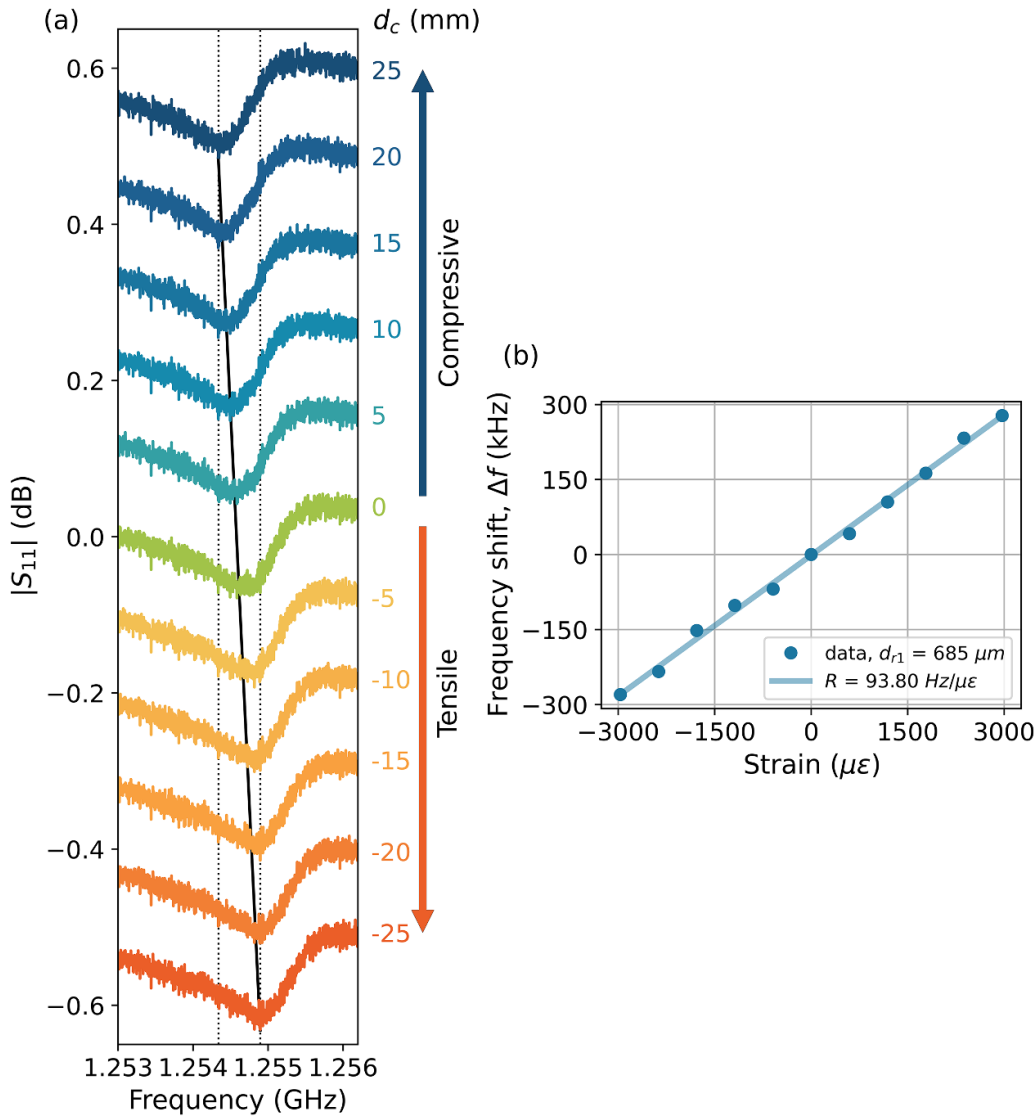


Figure 5. (a) Measured raw data of magnitude of reflection coefficient $|S_{11}|$ for different strain values in SAW. Positive values of the cantilever tip displacement d_c indicate compressive strain, while negative values indicate tensile strain, applied to device 1 at $x_0 = 30.0$ mm. The black solid line underneath the experimental data $|S_{11}|$ connects the two resonance frequencies when the strain is at its maximum and minimum values as gray dotted lines. Reproduced from [43]. © 2024 The Authors. CC BY 4.0. (b) The frequency shift of device 1 under applied strain value. SAW sensor responsivity R is $93.80 \text{ Hz} \mu\epsilon^{-1}$ in strain regime of $\pm 3560 \mu\epsilon$ range. The circles represent the experimental data from (a), and the solid line is a fit to this data. R is the slope of the linear fit function.

strain value. This is because, with a longer resonator, the path of the propagating SAWs is extended. As the SAWs propagate this extended path, they undergo more cumulative deformation from applied strain. This increased deformation amplifies the effect of the strain on resonance frequency, leading to more pronounced frequency shifts. Our results show that long resonators significantly improve responsivity, providing a way for optimizing SAW sensors for applications requiring high sensitivity.

However, this increase in responsivity R comes at the expense of decreasing linear output characteristics, as indicated by larger error bars shown in figure 6(c). These error bars represent the standard deviation of the slope of the fitted linear function, which corresponds to the responsivity R .

Notably, the largest error bar is observed for device 3, and upon examining figure 6(b), it is evident that $-3979 \mu\epsilon$, the data points deviate more significantly from the fitted linear function by approximately 120 kHz. Therefore, while longer resonator lengths may provide higher responsivities R , they also introduce nonlinearities into strain sensing.

3.4. Nonlinearity in longer resonator

From our experiments, we assume that nonlinearity begins to appear in the longer SAW resonators. To investigate this phenomenon, we first analyze the geometric and material nonlinearities and then assess the errors arising from fitting the experimental data. Geometric nonlinearity occurs when the

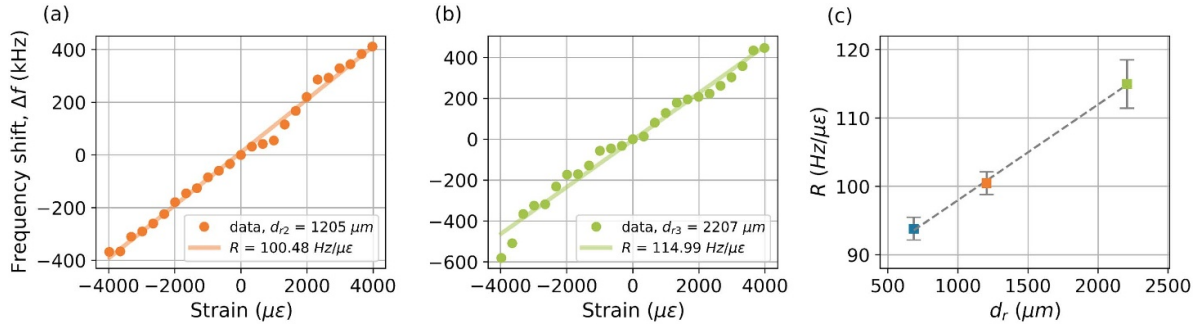


Figure 6. (a), (b) The frequency shift of device 2 and device 3 under applied strain value. SAW sensor responsivities R of (a) $100.48 \text{ Hz}\mu\epsilon^{-1}$ and (b) $114.99 \text{ Hz}\mu\epsilon^{-1}$ in strain regime of about $\pm 3979 \mu\epsilon$ range. The circles are the experimental data, and the solid line is a line fit to the data. R is the slope of the linear fit function. (c) Responsivity R as a function of different distances between the two reflectors d_r . The gray dash line is the linear fit function of the three devices. The gray error bars indicate the deviation of the data values from the linear fit function of the response shown in figures 5(b), 6(a), and (b). Reproduced from [43]. © 2024 The Authors. CC BY 4.0.

deformation of a structure is so large that it causes significant changes in shape. Specifically, we examine the effects of geometric nonlinearity by incorporating nonlinear terms into the strain equations. Additionally, we explore material nonlinearity, which occurs in solid mechanics when the relationship between stress and strain is no longer linear. We investigate whether variations in Young's modulus and residual stress in the AlN films might contribute to the observed nonlinearity. Lastly, we analyze the errors from the data fitting process to determine if non-linear effects play a major role.

In Euler–Bernoulli beam theory, where x is the coordinate along the length of the beam and u is the displacement in the x -direction, the longitudinal strain at the neutral axis of the beam is given by $\varepsilon = du/dx$. The strain ε at $x = x_0$ is obtained from equation (1) without considering any non-linear effects. Including geometric nonlinearity introduces additional terms to the equation. The strain equation considering nonlinearity following the basic nonlinear strain-displacement relationship, based on von Kármán strain theory [50], is given by:

$$\begin{aligned}\varepsilon_{\text{nonlinear}} &= \frac{du}{dx} + \frac{1}{2} \left(\frac{dw}{dx} \right)^2 \\ &= \varepsilon + \frac{1}{2} \left(\frac{dw}{dx} \right)^2, \\ \text{where } w &= \frac{d_c}{2L^3} (3Lx^2 - x^3).\end{aligned}\quad (3)$$

Here, z is the coordinate along the cantilever thickness and w is the displacement in the z -direction. To quantify the influence of the geometric nonlinearity in our setup, we compare the strain ε from equation (1) and $\varepsilon_{\text{nonlinear}}$ from equation (3) at $x = x_0$, where $d_c = 30 \text{ mm}$ and $x_0 = 10 \text{ mm}$. The influence of geometric nonlinearity is about 6% at the strain of approximately $-4000 \mu\epsilon$, calculated as the difference between $\varepsilon = -3979 \mu\epsilon$ and $\varepsilon_{\text{nonlinear}} = -3738 \mu\epsilon$. This comparison indicates that while a 6% influence is not dominant in the overall structural response, it is also not negligible. The small nonlinearities observed near strain of $-4000 \mu\epsilon$ in figure 6(b) could be attributed to the geometric nonlinearity we have calculated.

While geometric nonlinearity can be one factor, we have also considered other potential contributors to the observed nonlinearity. Material nonlinearity is related to properties such as Young's modulus [51]. As reported in [52], the study investigated how the thickness of sputter-deposited AlN films on Si substrates under conditions similar to ours affects both the residual stress and the Young's modulus. Young's modulus increases slightly from 232 to 248 GPa as the AlN film thickness increases from 600 to 1220 nm, showing a generally consistent value without significant variation. The residual stress in AlN films decreases from 350 MPa at 600 nm to 87 MPa at 1220 nm. In our SAW strain sensing, with an AlN film thickness of 1400 nm, the residual stress is less than 87 MPa as reported in [52]. While shorter resonators like device 1 and device 2 do not exhibit significant nonlinear behavior, the slight nonlinearity observed in longer resonators like device 3 could be more influenced by variations in material properties due to the longer path length. As the resonator length increases, even small variations in AlN film thickness can lead to changes in residual stress distribution, contributing to the observed nonlinearity. Thus, the longer resonator lengths might be more sensitive to these material property variations. Furthermore, stress variations in the adhesive layer (e.g. glue) under high strain could also play a role in the nonlinearity. However, quantifying the specific impact of the bonding material is challenging in our current setup and requires further investigation.

In the previous two paragraphs, we examine the causes of the observed nonlinearity from geometric and material factors. Here, we analyze the errors arising from fitting the experimental data to evaluate whether these errors indicate nonlinearity as shown in figure 6(b). Figure 7(a) shows all measured data of the magnitude of reflection coefficient $|S_{11}|$ in figure 6(b) respectively. The data are intentionally offset to clearly distinguish each frequency response when the displacement of the cantilever tip d_c changes by 2.5 mm. Figure 7(b) not only shows clearly how the resonance frequency shifts with an applied strain like figure 6(b), but also shows error bars which indicate the standard deviation errors of resonance frequencies from the fitted curve. Under negative

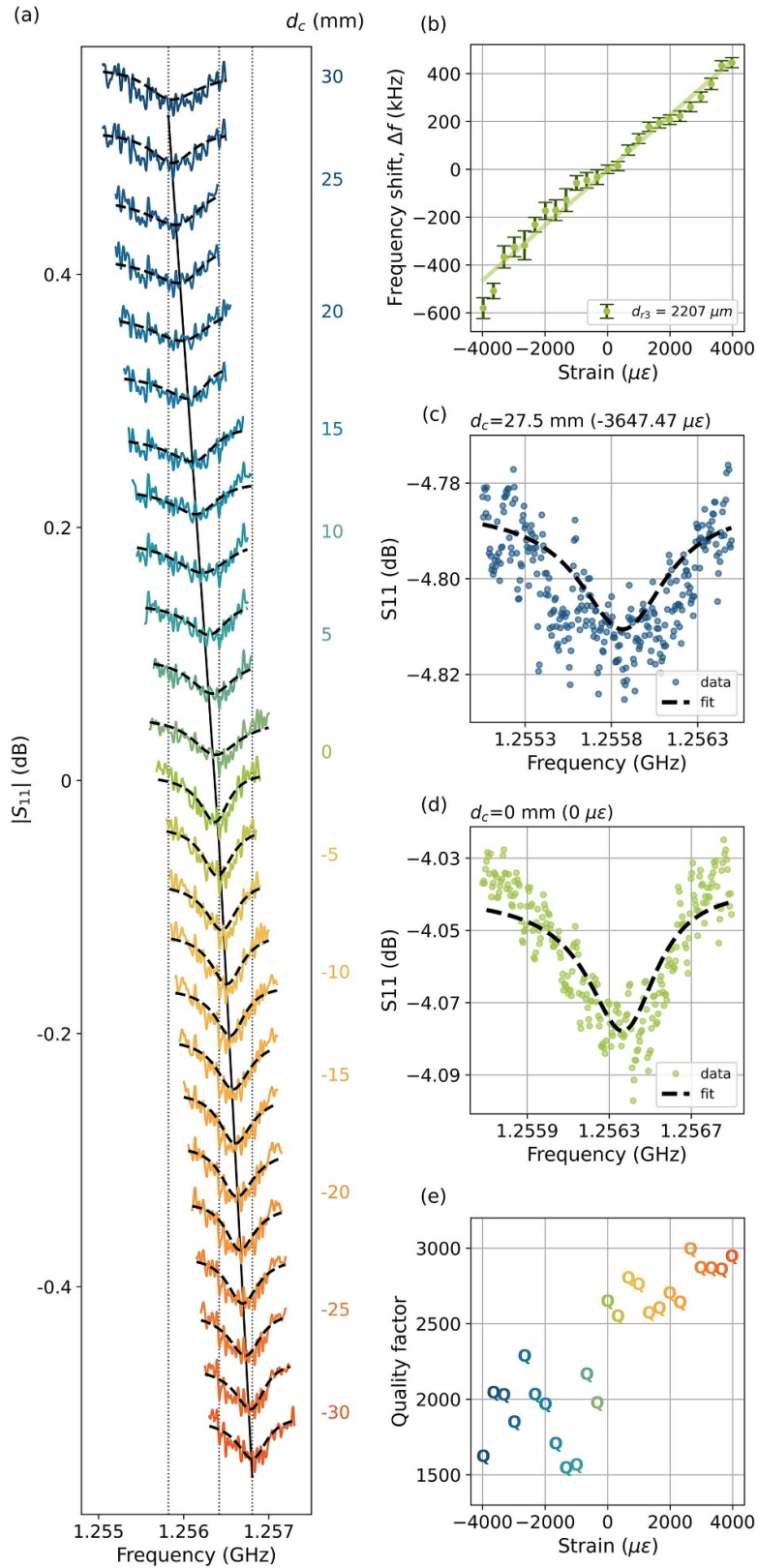


Figure 7. (a) Measured raw data of magnitude of reflection coefficient $|S_{11}|$ of Device 3 for different strain values in SAW. When the cantilever tip displacement d_c is from -30 mm to 30 mm is applied to Device 3 in table 1 with d_{r3} of $2207 \mu\text{m}$ at $x_0 = 10.0$ mm. The black dashed lines are the fitting curves from equation (2). The black solid line underneath the experimental data $|S_{11}|$ connects the three resonance frequencies when d_c is -30 mm, 0 mm, and 30 mm as gray dotted lines. (b) The frequency shift of Device 3 as green circles. Error bars indicate the standard deviation errors of each fitting parameter from the fitted curve in (a). The solid line is a linear fit to the data as the same in figure 6(b). (c), (d) Measured $|S_{11}|$ for Device 3 under strains of $\varepsilon = -3647 \mu\epsilon$ ($d_c = -27.5$ mm) and $\varepsilon = 0 \mu\epsilon$ ($d_c = 0$ mm), respectively. Blue and green circles are experimental data, and black solid lines are fitting curves. (e) Quality factors Q of Device 3 according to strain ε change.

(compressive) strain, larger error bars indicate higher uncertainty in the fitted resonance frequency. The standard deviation errors are calculated as the square root of the diagonal elements of the covariance matrix obtained from the fitting procedure, which reflects the uncertainties in the parameter estimates. Figure 7(c) shows raw data of the magnitude of reflection coefficient $|S_{11}|$ as circles and fitted curves as dashed lines with strain $\varepsilon = -3647 \mu\epsilon$. At this strain level, the data starts to deviate from the fitted linear function. The standard deviation error for the fitted resonance frequency, according to equation (2), is 32.32 kHz. In contrast, figure 7(d) presents the same with strain $\varepsilon = 0 \mu\epsilon$ and the standard deviation error for the fitted resonance frequency is 17.90 kHz. Notably, non-linearity is observed in this frequency shift where the error in the fitted resonance frequency increases.

We capture the broadening bandwidth of the reflection coefficient $|S_{11}|$ when compressive strain is applied, as shown in figure 7(a), and compare the total quality factors Q for each dataset in figure 7(e). There is a clear trend showing that the total quality factor Q improves with the application of tensile strain. This indicates that the SAW resonator experiences less energy loss and potentially stores more energy under tensile compared to compressive strain. The quality factor Q of a resonator is significantly influenced by external conditions, such as the strain applied to the resonator. One important concept in understanding this behavior is thermoelastic damping, which refers to the energy loss due to the interaction between thermal and elastic deformations in the material. In mechanically highly stressed micro/nano resonators, thermoelastic damping plays a crucial role [51]. Additionally, repeated thermal stress associated with thermoelastic damping can contribute to the formation of micro-defects over time. When tensile stress is applied to the material, it can reduce existing micro-defects, thus decreasing energy loss pathways and increasing the quality factor Q . Conversely, compressive strain can increase micro-defects within the structure, leading to higher energy loss. Our results confirm that SAW strain sensors exhibit improved performance under tensile strain conditions. This suggests that SAW strain sensors can be practically utilized under tensile rather than compressive strain conditions.

Our investigation into the nonlinearity of longer SAW resonators reveals that geometric and material nonlinearity variations and fitting errors contribute to the observed behavior under high mechanical loading conditions. Geometric nonlinearity, though not dominant, shows about a 6% influence at high strain levels, suggesting its role in the slight deviations observed near $-4000 \mu\epsilon$. Material nonlinearity, particularly due to potential variations in residual stress distribution and AlN film thickness, may also play a role, with longer resonators potentially being more sensitive to these variations. The fitting errors indicate increased uncertainty under compressive strain, further highlighting the nonlinearity in the frequency response. Our analysis of the total quality factor Q demonstrates improved performance under tensile strain.

3.5. Benchmarks

The AlN-based SAW strain sensors investigated in this study at a resonance frequency of 1.25 GHz and show a responsivity R of $114.99 \text{ Hz } \mu\epsilon^{-1}$ in a strain regime of $\pm 3979 \mu\epsilon$. We compare the performance of our SAW strain sensors with those reported in literature, as shown in table 2. While most papers on SAW strain sensing have studied the resonance frequency within the MHz range, we show SAW strain sensing operating at the higher frequency range as GHz. Both resonator and delay line types of SAW sensors have been studied previously with a similar focus. In our setup, the strain regime reaches up to $\pm 3979 \mu\epsilon$, which is the highest in strain sensing studies compared to data reported in the literature. This excludes cases where flexible materials are utilized, as shown in figure 8, which visualizes the data from table 2.

The typical piezoelectric materials used in SAW strain sensors are quartz, LiNbO₃, ZnO, Languisite (LGS), and AlN. The SAW performance is affected depending on how the crystals of the piezoelectric material are aligned or cut, and on which substrate they are integrated. For example, quartz-based strain sensors with 36° AT-X cut [33] and 42.75° ST cut [53] are fabricated with similar designs as resonator types and resonance frequencies of 433 and 438 MHz. However, when using quartz with 42.75° ST cut, the responsivity R to strain is $551 \text{ Hz } \mu\epsilon^{-1}$ which is more than twice as large as the responsivity R of $241 \text{ Hz } \mu\epsilon^{-1}$ using the quartz with 36° AT-X cut. Among AlN-based strain sensors, our sensor and the strain sensor reported in [34] on a Si-based substrate have similar responsivity R of 115 and $107 \text{ Hz } \mu\epsilon^{-1}$, respectively. However, AlN strain sensors on polymeric and TC4 substrates [60, 61] have higher responsivities R of 577 and $402 \text{ Hz } \mu\epsilon^{-1}$, respectively. These comparisons highlight the competitive performance of our AlN-based SAW strain sensors on a Si-based non-flexible substrate, demonstrating its potential for highly accurate strain sensing applications.

As shown in table 2 and figure 8, the lowest responsivity R of $20 \text{ Hz } \mu\epsilon^{-1}$ is reported for the LGS-based sensor [37], while the highest responsivity R of $577 \text{ Hz } \mu\epsilon^{-1}$ is reported for the AlN-based sensor [60]. Our AlN-based strain sensor has the responsivity R of $115 \text{ Hz } \mu\epsilon^{-1}$ which is within the range of responsivity values as data reported in the literature.

4. Conclusion

In this article, we investigate the performance of GHz SAW resonators as strain sensors. Using a custom-built bendable cantilever setup, we applied controlled mechanical strains of up to $\pm 3979 \mu\epsilon$. Our results demonstrate that these sensors can detect shifts in resonance frequency under high mechanical strains. GHz SAW resonators for strain sensing are fabricated on a Si substrate using photolithography techniques. The resonance frequency and total quality factor Q of the SAW resonator without applied strain are 1.25 GHz and 1683, respectively. The experimental data shows a linear relationship between strains and frequency shift Δf , with a responsivity R

Table 2. Comparison of strain SAW sensing performance with different piezoelectric materials.

Materials	Resonance frequency (MHz)	Responsivity R (Hz $\mu\epsilon^{-1}$)	Strain regime ($\mu\epsilon$)	Type	Reference
Quartz plates with 36° AT-X cut*	260	252	1 to 5000	Delay line	[21]
Quartz substrate with 36° AT-X cut	433	241	50 to 400	Resonator	[33]
Quartz substrate with 42.75° ST cut	438	551	0 to 400	Resonator	[53]
LiNbO ₃ substrate with 128° YX cut	98	−103	0 to 62	Delay line	[54]
LiNbO ₃ substrate with 128° YX cut	151	126	0 to 400	Delay line	[32]
LiNbO ₃ film with 128° Y cut*	325	193	−3500 to 3500	Delay line	[20]
ZnO film on PET*	111	130	0 to 2500	Delay line	[55]
ZnO film*	133	35	−3000 to 3000	Delay line	[56]
ZnO film*	138	137	0 to 3000	Delay line	[57]
LGS film with a 3rd Euler angle of 117° on Si substrate *	153	45	1 to 1800	Resonator	[39]
LGS substrate with a 3rd Euler angle of 117°	169	20	0 to 500	Resonator	[37]
LGS substrate with a 3rd Euler angle of 26.7°	196	−41	0 to 100	Resonator	[58]
LGS substrate with a 3rd Euler angle of 26.6° †	225	143	0 to 700	Resonator	[35]
LGS substrate with a 3rd Euler angle of 32.9°	311	−182	0 to 250	Resonator	[59]
LGS film with a 3rd Euler angle of 72° on Si substrate	400	350	0 to 1200	Resonator	[38]
AlN film on SiO ₂ /Si substrate	108	107	0 to 90	Resonator	[34]
AlN film on polymeric substrate*	190	577	0 to 181	Delay line	[60]
AlN film on TC4 substrate	249	402	0 to 400	Resonator	[61]
AlN film*	290	180	0 to 1332	Delay line	[62]
AlN film on Si substrate	1225	115	−3979 to 3979	Resonator	This work

*indicates flexible material.

† indicates the SAWs propagate at an orientation of 30° to the applied strain.

PET: polyethylene terephthalate.

polymeric substrate: polymeric polyethylene naphthalate substrate.

TC4: titanium alloy (Ti–6Al–4V).

Euler angles for LGS include a first angle of 0° and a second angle of 138.5°.

of 93.80 Hz $\mu\epsilon^{-1}$ within a strain range of $\pm 3560 \mu\epsilon$. Moreover, our study reveals a correlation between resonator length and responsivity, as longer resonators achieved higher responsivity within a strain range of $\pm 3979 \mu\epsilon$. It is observed that longer resonator lengths resulted in higher responsivities, with R values of 100.48 and 114.99 Hz $\mu\epsilon^{-1}$ for reflector distances of 1205 and 2207 μm , respectively. However, nonlinearity is observed in longer resonators especially under compressive strain. Additionally, the total quality factor Q decreased under compressive strain, suggesting that SAW strain sensors are better utilized under tensile strain conditions for improved performance.

This study focuses on the fundamental performance of GHz SAW strain sensors under high mechanical strain conditions, demonstrating their stable responsivity under extreme loading on non-flexible substrates. While optimization for a specific application is beyond the scope of this work, these findings show the high potential of GHz SAW resonators for advanced sensor applications. In the near future, further investigations will focus on investigating the impact of non-linear effects on device performance under high-loading conditions, thus

paving the way for new applications of compact and low-power SAW strain sensors such as needed in structural health monitoring applications and wireless sensor networks.

Figure 9 illustrates how SAW strain sensors can be applied in structural health monitoring systems. In aircraft, sensors can monitor high-stress areas such as the wing-fuselage junction, with data transmitted wirelessly to onboard reader units installed within the aircraft's monitoring systems for real-time analysis. Similarly, in buildings and bridges, these sensors detect strain in critical load-bearing structures, with reader units positioned centrally such as maintenance hubs to aggregate data. The collected data is transmitted to a centralized monitoring system, where the resonance frequency shifts (Δf) caused by strain are analyzed to detect and quantify potential damage. While this study employs a simple SAW resonator design for one-port measurements at fundamental physics, future collaboration with antenna-based strain sensing mechanisms [63, 64], machine learning algorithms for predictive analysis [65], and real-time data computing technologies [66, 67] could significantly enhance its application potential.

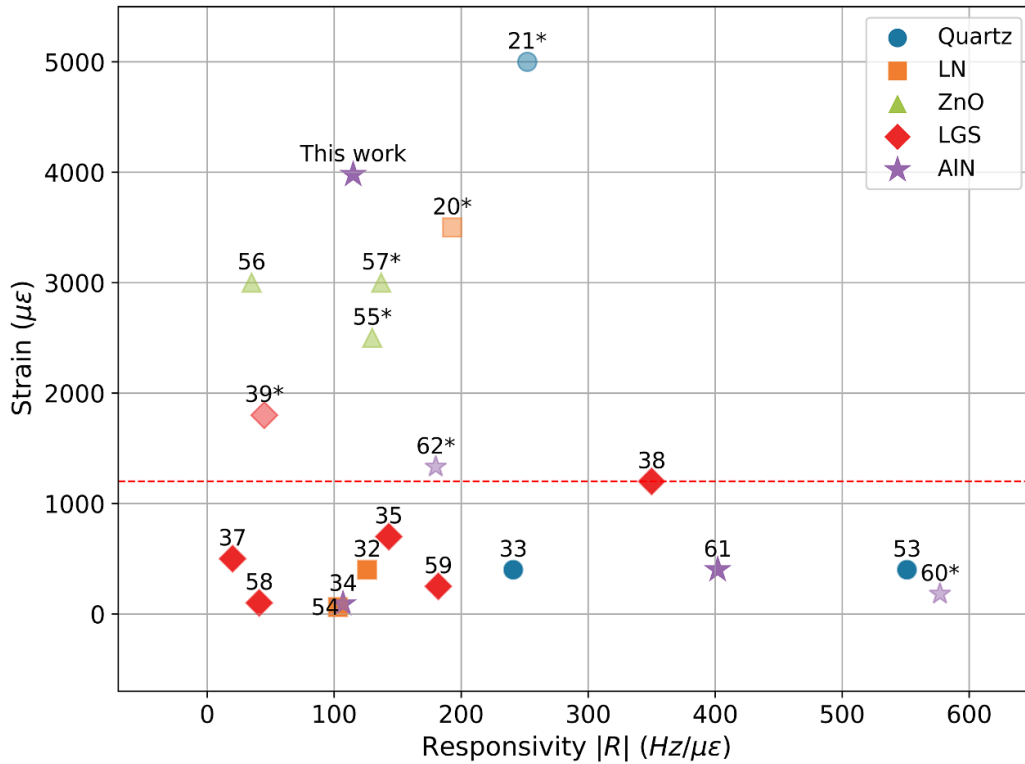


Figure 8. Correlation of absolute value of responsivity $|R|$ and strain on different piezoelectric materials. Numbers on the data are reference numbers from table 2 and * indicates flexible material. The maximum strain applied is $1200 \mu\epsilon$ which is indicated as the red dashed line among strain on different piezoelectric materials except flexible material and this work’s material.

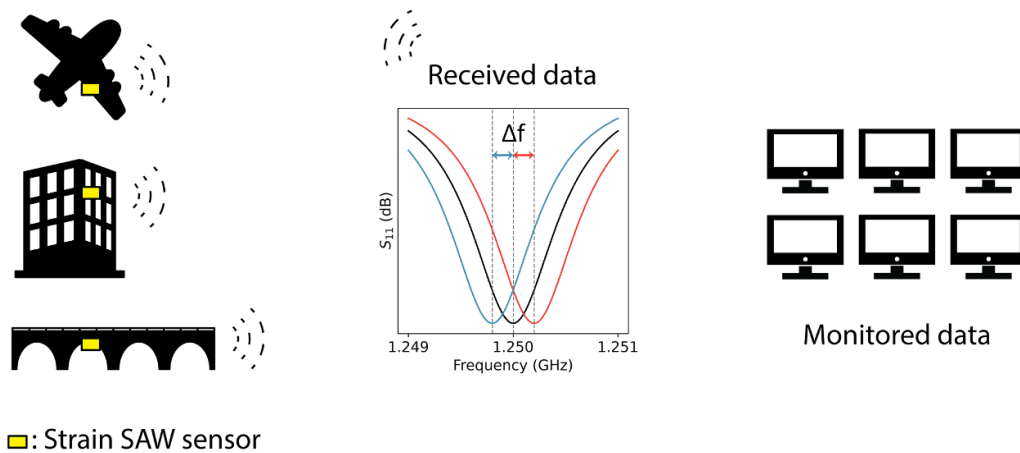


Figure 9. Illustration of a structural health monitoring system integrating SAW strain sensors for real-time strain detection and analysis.

Data availability statement

The data cannot be made publicly available upon publication because no suitable repository exists for hosting data in this field of study. The data that support the findings of this study are available upon reasonable request from the authors.

Acknowledgments

The authors acknowledge TU Wien Bibliothek for financial support through its Open Access Funding Programme. This project has received funding from the European Union’s

Horizon 2020 research and innovation programme as project ‘Quantum-Limited Atomic Force Microscopy’ (www.qafm.eu) under Grant Agreement No. 828966 (<https://cordis.europa.eu/project/id/828966>).

ORCID iDs

MinHee Kwon <https://orcid.org/0000-0001-5997-1547>
 Matthias Schlögl <https://orcid.org/0000-0003-1226-6570>
 Daniel Platz <https://orcid.org/0000-0002-5923-0279>
 Ulrich Schmid <https://orcid.org/0000-0003-4528-8653>

References

- [1] Hamed Y, O'Donnell G, Lishchenko N and Munina I 2023 *IEEE Sens. J.* **23** 25618–49
- [2] Guo H, Xiao G, Mrad N and Yao J 2011 *Sensors* **11** 3687–705
- [3] Guo J, Zhou B, Zong R, Pan L, Li X, Yu X, Yang C, Kong L and Dai Q 2019 *ACS Appl. Mater. Interfaces* **11** 33589–98
- [4] Wu T, Liu G, Fu S and Xing F 2020 *Sensors* **20** 4517
- [5] Cai L et al 2013 *Sci. Rep.* **3** 3048
- [6] Choi T Y, Hwang B U, Kim B Y, Trung T Q, Nam Y H, Kim D N, Eom K and Lee N E 2017 *ACS Appl. Mater. Interfaces* **9** 18022–30
- [7] Qiu A, Li P, Yang Z, Yao Y, Lee I and Ma J 2019 *Adv. Funct. Mater.* **29** 1806306
- [8] Trolier-McKinstry S and Murali P 2004 *J. Electroceramics* **12** 7–17
- [9] Bu G, Ciplys D, Shur M, Schowalter L, Schujman S and Gaska R 2006 *IEEE Trans. Ultrason. Ferroelectr. Freq. Control* **53** 251–4
- [10] Al Ahmad M and Plana R 2009 *Int. J. Microw. Wirel. Technol.* **1** 5–9
- [11] Ye X, Fang L, Liang B, Wang Q, Wang X, He L, Bei W and Ko W H 2011 *Sens. Actuators A* **169** 74–82
- [12] Shu L, Peng B, Yang Z, Wang R, Deng S and Liu X 2015 *Sensors* **15** 28531–42
- [13] Kim S, Adib M R and Lee K 2019 *Sens. Actuators A* **297** 111549
- [14] Wang W, Xue X, Fan S, Liu M, Liang Y and Lu M 2020 *Sens. Actuators A* **308** 112015
- [15] Oh H, Lee K, Eun K, Choa S H and Yang S S 2012 *J. Micromech. Microeng.* **22** 025002
- [16] Wilson W C and Juarez P D 2014 *Proc. Comput. Sci.* **37** 101–8
- [17] Ren J, Anurakparadorn K, Gu H, Zhao M and Wei X 2018 *Microsyst. Technol.* **25** 351–9
- [18] Wang X, Du L, Cheng L, Zhai S, Zhang C, Wang W, Liang Y, Yang D, Chen Q and Lei G 2022 *Sens. Actuators B* **351** 130952
- [19] Mengue P et al 2023 *Smart Mater. Struct.* **32** 095017
- [20] Xu H, Dong S, Xuan W, Farooq U, Huang S, Li M, Wu T, Jin H, Wang X and Luo J 2018 *Appl. Phys. Lett.* **112** 093502
- [21] Feng B, Jin H, Fang Z, Yu Z, Dong S and Luo J 2021 *IEEE Sens. J.* **21** 18571–7
- [22] Li X, Tan Q, Qin L, Yan X and Liang X 2022 *Micromachines* **13** 912
- [23] Yim W M and Paff R J 1974 *J. Appl. Phys.* **45** 1456–7
- [24] Slobodnik A 1976 *Proc. IEEE* **64** 581–95
- [25] Lakin K, Belsick J, McDonald J and McCarron K 2001 *2001 IEEE Ultrasonics Symp. Proc. Int. Symp. (Cat. No.01CH37263)*
- [26] Kwon M, Ignat I, Platz D, Arthaber H and Schmid U 2023 *Sens. Actuators A* **362** 114637
- [27] Humphries J R and Malocha D C 2015 *IEEE Sens. J.* **15** 5527–34
- [28] Furniss J, Carka D, Voiculescu I, Lee K L, Xiang D and Li F 2018 *2018 6th IEEE Int. Conf. on Wireless for Space and Extreme Environments (WiSEE)* vol **139** pp 206–11
- [29] Morales Otero M J and Malocha D C 2023 *IEEE J. Radio Freq. Identif.* **7** 379–89
- [30] Hu B, Zhang S, Zhang H, Lv W, Zhang C, Lv X and San H 2019 *Micromachines* **10** 349
- [31] Chen J et al 2015 *J. Micromech. Microeng.* **25** 115005
- [32] Fu C, Lee K, Lee K, Yang S S and Wang W 2014 *Sens. Actuators A* **218** 80–87
- [33] Stoney R, Geraghty D and O'Donnell G E 2014 *IEEE Sens. J.* **14** 722–8
- [34] Bao Z, Hara M and Kuwano H 2015 *2015 Transducers—2015 18th Int. Conf. on Solid-State Sensors, Actuators and Microsystems (TRANSDUCERS)*
- [35] Li L, Peng B, Zhu J, He Z, Yang Y and Zhang W 2021 *IEEE Sens. J.* **21** 4688–95
- [36] Hu F, Cheng L, Fan S, Xue X, Liang Y, Lu M and Wang W 2022 *Sens. Actuators A* **333** 113298
- [37] Yan X, Tan Q, Li X, Xue T and Li M 2022 *IEEE Sens. J.* **22** 12622–8
- [38] Zhang J, Jin H, Dong S, Ding R, Chen J, Xuan W, Gao F and Luo J 2022 *IEEE Sens. J.* **22** 11509–16
- [39] Li X, Qin L, Guo L and Tan Q 2023 *IEEE Sens. J.* **23** 18022–31
- [40] Zhou J, Ji Z, Guo Y, Liu Y, Zhuo F, Zheng Y, Gu Y, Fu Y and Duan H 2022 *npj Flex. Electron.* **6** 55
- [41] Ababneh A, Alsumady M, Seidel H, Manzanique T, Hernando-García J, Sánchez-Rojas J, Bittner A and Schmid U 2012 *Appl. Surf. Sci.* **259** 59–65
- [42] Schlögl M, Köpl S, Hiesberger J, Schneider M and Schmid U 2022 *Sens. Actuators A* **346** 113829
- [43] Kwon M, Schlögl M, Platz D and Schmid U 2024 *EUROSENSORS XXXVI (Lectures)* pp 67–68
- [44] Bauchau O A and Craig J I 2009 *Euler–Bernoulli beam theory Structural Analysis* (Springer) pp 173–221
- [45] Morgan D 2010 *Surface Acoustic Wave Filters: With Applications to Electronic Communications and Signal Processing* (Academic)
- [46] Aref T, Delsing P, Ekström M K, Kockum A F, Gustafsson M V, Johansson G, Leek P J, Magnusson E and Manenti R 2016 *Superconducting Devices in Quantum Optics* (Springer) pp 217–44
- [47] Caliendo C and Imperatori P 2003 *Appl. Phys. Lett.* **83** 1641–3
- [48] Abdolvand R, Lavasani H, Ho G and Ayazi F 2008 *IEEE Trans. Ultrason. Ferroelectr. Freq. Control* **55** 2596–606
- [49] Lavasani H M, Pan W and Ayazi F 2010 *2010 IEEE Radio Frequency Integrated Circuits Symp.*
- [50] Ma H, Gao X and Reddy J 2008 *J. Mech. Phys. Solids* **56** 3379–91
- [51] Schmid S, Villanueva L G and Roukes M L 2023 *Fundamentals of Nanomechanical Resonators* (Springer)
- [52] Schneider M, Bittner A and Schmid U 2014 *Appl. Phys. Lett.* **105** 201912
- [53] Ma X, Xiao Q, Fan Y, Yu X and Ji X 2022 *IEEE Sens. J.* **22** 12595–601
- [54] Kelly L, Chen C, Bao X and Berini P 2022 *Sens. Actuators A* **338** 113504
- [55] He X, Guo H, Chen J, Wang W, Xuan W, Xu Y and Luo J 2014 *Appl. Phys. Lett.* **104** 213504
- [56] Chen J, He X, Wang W, Xuan W, Zhou J, Wang X, Dong S R, Garner S, Cimo P and Luo J K 2014 *J. Mater. Chem. C* **2** 9109–14
- [57] Chen J, Wang W, Xuan W, Wang X, Dong S, Garner S, Cimo P and Luo J 2016 *MRS Adv.* **1** 1519–24
- [58] Maskay A and da Cunha M P 2017 *Sens. Actuators A* **259** 34–43
- [59] Jilani S F, Leff D, Maskay A, Lad R J and da Cunha M P 2020 *2020 IEEE Int. Ultrasonics Symp. (IUS)*
- [60] Lamanna L, Rizzi F, Guido F and De Vittorio M 2020 *IEEE Electron Device Lett.* **41** 1692–5

- [61] Shu L, Wang X, Li L, Yan D, Peng L, Fan L and Wu W 2019 *Sens. Actuators A* **293** 14–20
- [62] Ji Z, Zhou J, Lin H, Wu J, Zhang D, Garner S, Gu A, Dong S, Fu Y and Duan H 2021 *Microsyst. Nanoeng.* **7** 97
- [63] Zhang Q, Wang Y, Li D, Xie J, Tao K, Hu P, Zhou J, Chang H and Fu Y 2022 *Adv. Funct. Mater.* **33** 2209667
- [64] Dyogi J, Song X, Jang S H, Nam S H and Cho C 2023 *Eng. Proc.* **36** 53
- [65] Ji Z, Zhou J, Guo Y, Xia Y, Abkar A, Liang D and Fu Y 2024 *Microsyst. Nanoeng.* **10** 94
- [66] Babu V J, Anusha M, Sireesha M, Sundarrajan S, Abdul Haroon Rashid S S A, Kumar A S and Ramakrishna S 2022 *Polymers* **14** 2219
- [67] Wong V K, Rabeek S M, Lai S C, Philibert M, Lim D B K, Chen S, Raja M K and Yao K 2022 *Sensors* **22** 5724